# Estimating weakening on hillslopes caused by strong earthquakes

Check for updates

Chuanjie Xi[1,2], Hakan Tanyas [2] ✉, Luigi Lombardo [2], Kun He[1], Xiewen Hu[1] & Randall W. Jibson [3]

The weakening of hillslopes during strong earthquakes increases landsliding rates in post-seismic periods. However, very few studies have addressed the amount of coseismic reduction in shear strength of hillslope materials. This makes estimation of post-seismic landslide susceptibility challenging. Here we propose a method to quantify the maximum shear-strength reduction expected on seismically disturbed hillslopes. We focus on a subset of the area affected by the 2008 $M_w$ 7.9 Wenchuan, China earthquake. We combine physical and data-driven modeling approaches. First, we back-analyze shear-strength reduction at locations where post-seismic landslides occurred. Second, we regress the estimated shear-strength reduction against peak ground acceleration, local relief, and topographic position index to extrapolate the shear-strength reduction over the entire study area. Our results show a maximum of 60%–75% reduction in near-surface shear strength over a peak ground acceleration range of 0.5–0.9 g. Reduction percentages can be generalized using a data-driven model.

Earthquakes and rainfall are the most common triggers of landslides. Thus, many papers have been published regarding their hazardous consequences on slope stability[1–4] and their influences on landscape evolution[5–9]. Global predictive models separately exist for both earthquake- and rainfall-triggered landslides[10,11]. However, few predictive models include the compound effects of earthquakes and rainfall, and they are only available for specific areas, where both multi-temporal landslide inventories and proxies representing the triggering factors exist[12].

The predictive capacity of models targeting landslides is limited primarily by the accuracy of model inputs and, in particular, the availability of landslide inventories and estimates of triggering factors[13]. Use of physical models decreases the strong data dependency with respect to landslide inventories, but characterizing shear strength at global and regional scales remains challenging[14]. But if the geotechnical characteristics of hillslopes, as well as the triggering factors of rainfall and seismic shaking, can be reasonably estimated, hazard from earthquake- and rainfall-triggered landslides can be modeled[15–18]. Nevertheless, identifying the compound effect of earthquakes and rainfall is still difficult[19]. For example, modeling hazard from rainfall-triggered landslides in an area recently struck by an earthquake requires a better understanding because post-seismic hillslope susceptibility varies mainly depending on landslide characteristics (e.g., type of landslide material, slope, and landslide geometry) and the mechanism controlling strain accumulation within the landslide body[19,20].

Further complicating matters is that laboratory-scale analyses show that post-seismic hillslope strength can be unchanged, increased, or decreased compared to its pre-seismic counterpart[19,20]. Most commonly, however, strong ground shaking weakens hillslopes[21,22]. This weakening, which is also observed in regional-scale assessments using multi-temporal landslide inventories[23–26], commonly is referred to as the earthquake legacy effect[27–29]. The magnitude and duration of the legacy effect can be estimated by examining reactivated or new landslides that occur in post-seismic periods[29,30].

Coseismic hillslope weakening is caused by ground shaking that disturbs hillslopes whether or not landslides are triggered. This disturbance can cause a reduction in shear strength (RSS) of hillslope materials. To accurately characterize the resultant elevated landslide susceptibility in post-seismic periods using physical modeling, the amount of RSS needs to be estimated. Theoretically, this could be done by detailed geotechnical characterization of hillslope material in pre- and post-seismic periods. In this context, type of hillslope materials, hillslope geometry, and failure surface[31,32] also need to be characterized. As a result of such investigations, the most appropriate failure criterion is selected for a given hillslope to estimate its strength. For instance, the stability of a hillslope governed by soil, intact rock, or discontinuities could be assessed by using Mohr-Coulomb[33], Hoek-Brown[34,35], and Barton-Bandis[36,37] failure criteria, respectively. However, in regional-scale analyses, such detailed geotechnical investigations on a regional scale are impractical because of the time and cost required.

[1]Southwest Jiaotong University, Faculty of Geoscience and Environmental Engineering, Chengdu, China. [2]University of Twente, Faculty of Geo-Information Science and Earth Observation (ITC), Enschede, The Netherlands. [3]Independent researcher, retired from Geologic Hazards Science Center, U.S. Geological Survey, Golden, CO, USA. ✉e-mail: h.tanyas@utwente.nl

To address these limitations, some methods coupling active geotechnical seismic surveys with outcrop-scale engineering desciptions/tests, which are used to classify rock masses based the geological strength index[34], have been proposed[38,39]. However, even those methods fail to capture slope shear strength at a regional scale and thus do not address the RSS.

In light of these limitations of physical sampling and testing, we aim to capture the amount of RSS of hillslope materials following strong earthquakes by carrying out back analyses[40–42]. To do so, we analyze a subset of the area affected by the 2008 $M_w$ 7.9 Wenchuan, China earthquake[43]. The earthquake triggered ~200,000 landslides around the Longmen mountains[44]. In addition to triggering widespread coseismic slope failures, the earthquake also increased the post-seismic landslide frequency[21,25,45]. Although it was argued that the legacy effect of the earthquake on hillslope stability could last several decades[24], a study of the epicentral area of the where peak ground acceleration (PGA) ranged from 0.4 g–1.0 g suggested that the legacy effect lasted ~7 years[46]. In this study, we focus on the same area (Fig. 1)[47].

Landslides that occurred in our study area were mapped by Fan et al.[43,48]. They generated one coseismic and five post-seismic landslide inventories obtained by comparing successive images acquired in 2011, 2013, 2015, 2017, and 2018 (Supplementary Fig. 1). They assessed the average uncertainty in landslide polygons as ± 19 % in terms of total landslide area based on comparison between five geomorphologists that mapped the same area. They mapped remobilized landslides and new landslides triggered in post-seismic periods of the 2008 Wenchuan earthquake. We exclude remobilized landslides from our analyses because we lack access to multi-temporal digital elevation models (DEMs) of hillslope geometry before and after the remobilization. Considering remobilized cases would introduce additional uncertainties in the back-analysis. Therefore, we focus exclusively on coseismic landslides and the newly activated ones that occurred post-seismically (Supplementary Table 1) to estimate the RSS responsible for their initiation.

To estimate the shear strength of slope materials, we limit our study area to locations where post-seismic landslides occurred. Specifically, we back-analyze unfailed hillslopes during the coseismic event and both unfailed and failed hillslopes in the post-seismic periods. By doing so, we aim to estimate shear strength at locations where hillslopes did not fail in the coseismic event but rather in one of the post-seismic periods. We then calculate the RSS, which represents the decrease between the shear strength in the coseismic and post-seismic periods. Ultimately, we analyze the spatial distribution of RSS in relation to topographic and seismic variables using a data-driven model (Gaussian Generalized Linear Model, GLM) and extrapolate estimated reductions over larger areas. Our findings provide a comprehensive insight into post-seismic hillslope reaction to strong ground shaking.

## Results

### Estimating strength parameters

The study area includes five lithologic units (National Geological Data Library of China Geological Survey, http://www.ngac.org.cn): andesite, phyllite and schist, lithic sandstone, granite, and diorite (Fig. 1). To estimate shear strengths of these lithologic units, we estimate the average landslide thickness in the study area. We use published landslide area-volume relationships for landslide thicknesses as great as 5 m (Fig. 2)[49,50]. We include a sensitivity test for a range of potential values (2 m, 3 m, 4 m, and 5 m) to be separately introduced in our back-analytical routine[51,52].

For each post-seismic landslide location, we assign material and shear-strength properties ($\gamma$, $\varphi'$, $c'$) to each grid cell (Table 1) based on published values corresponding to the five lithologic units in the area[14,15,53–56]. For the identified range of cohesion and friction-angle couples, we iteratively test shear-strength values from the literature that meet the failure and stability conditions for both coseismic and post-seismic periods. Figure 3 shows an example for granite hillslopes where landslide thickness is 3 m. We run the same analyses for each lithologic unit for the four landslide thicknesses (see Supplementary Fig. 2).
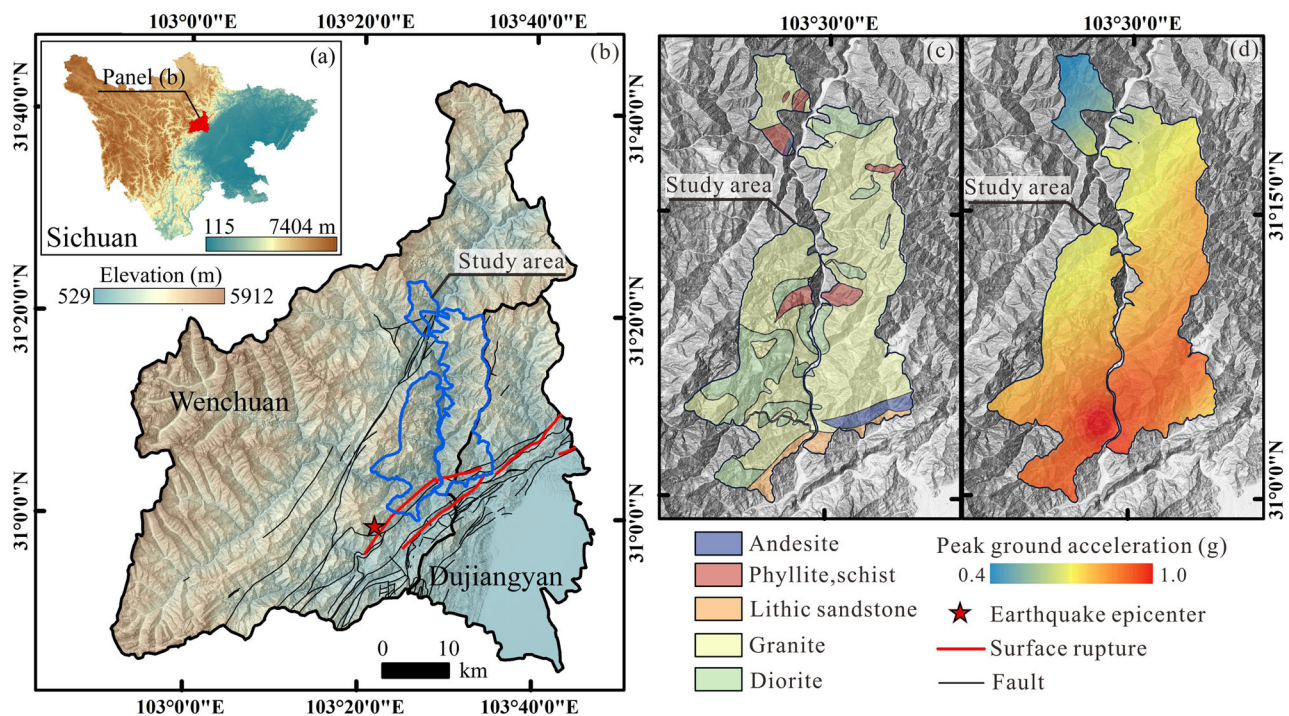


**Fig. 1 | Maps showing the study area. a** Location map. **b** Study area overlain by faults and earthquake epicenter. **c** Major geologic units in study area. **d** Peak ground acceleration map of the 2008 Wenchuan earthquake bounded by the study area.

Surface rupture is digitized from Xu et al.[47] and geologic map is taken from National Geological Data Library of China Geological Survey (http://www.ngac.org.cn).
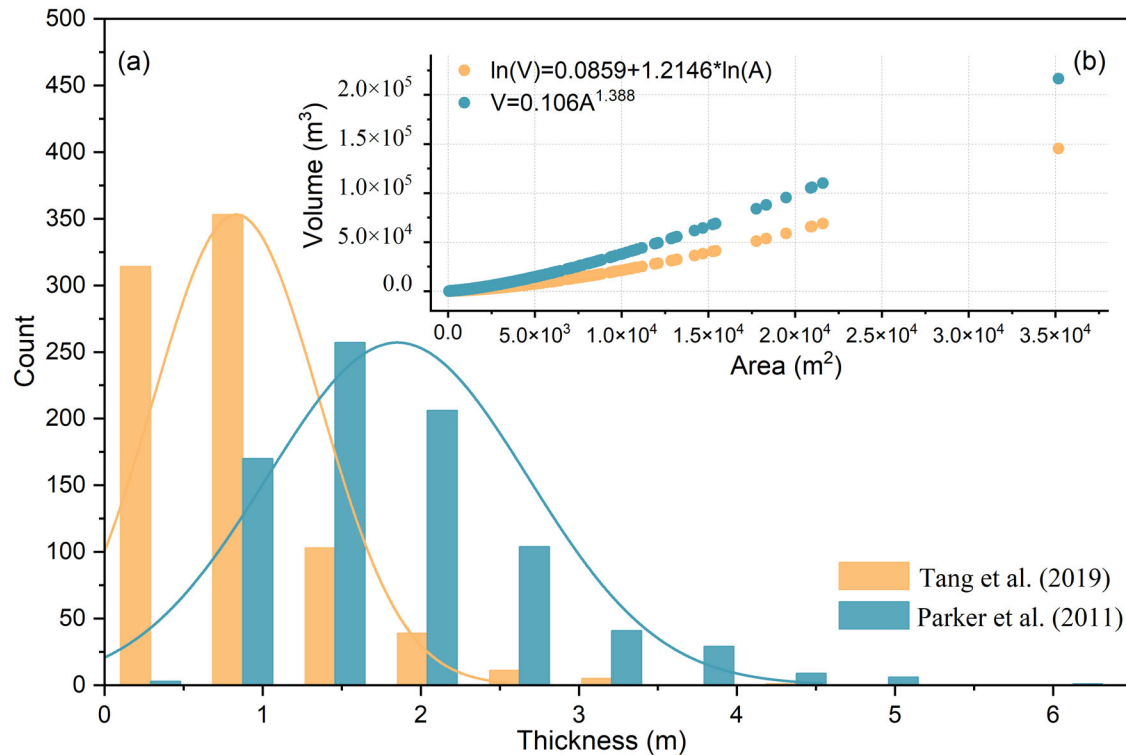
**Fig. 2 | Estimated landslide thickness based on two landslide area-volume relationships proposed for the landslides triggered by the Wenchuan earthquake. a** Landslide thickness distribution. **b** Curves representing the landslide area-volume relationship.

## Estimating RSS

The approach presented above allows us to identify the mean shear strength of hillslope materials for post-seismic landslide locations in both coseismic and post-seismic periods. We then compare these post-seismic shear strengths with their coseismic counterparts and calculate the difference, which yields the RSS due to the earthquake.

Seismic ground motion in the study area ranged from 0.4 g–1.0 g; thus, we calculate the RSS of hillslopes across this range (Fig. 4). Figure 4a shows that the RSS ranges from 40–80 kPa where the landslide thickness is 2 m. Results also show that the RSS is positively correlated with PGA. This indicates that hillslopes affected by stronger ground shaking have higher RSS in post-seismic periods. We also show that greater RSS is required for deeper landslides to fail. For example, for a landslide thickness of 5 m, the estimated RSS is 120–180 kPa (Fig. 4d), whereas its counterpart for a landslide thickness of 2 m is 40–80 kPa. This does not mean that the percentage of RSS is necessarily higher for deeper landslides because this amount changes depending on the initial shear strength in the coseismic phase. Shear strength along the failure surface increases as the thickness of a landslide increases because of increasing normal stress at depth. Therefore, a higher RSS is required to cause failure of a deeper landslide.

## Table 1 | Cohesion and friction-angle couples for the five lithologic units

| Lithology | Cohesion (kPa) | Friction angle (°) |
|---|---|---|
| Andesite | 39 | 42 |
| Phyllite, schist | 27 | 35 |
| Lithic sandstone | 29 | 39 |
| Granite | 40 | 44 |
| Diorite | 40 | 43 |

These values are used as mean values to build a Gaussian distribution to estimate a range of values fulfilling the required stability and failure conditions. Lithologic descriptions are taken from the National Geological Data Library of China Geological Survey, http://www.ngac.org.cn.

To express RSS in terms of percentages, we compare them with their coseismic counterparts (Fig. 5). Results show that for all thicknesses, RSS generally varies between 60% and 75% (Fig. 5e).

## Extrapolating RSS through a data-driven model

This stage of the analysis estimates RSS only within mapped coseismic landslides because we lack information about unfailed slopes. Therefore, we include a final step aimed at regionalizing the RSS model. We use a Gaussian Generalized Linear Model (GLM) trained to explain the spatial variability in RSS as a function of PGA, local relief (LR), and topographic position index (TPI). Because the RSS model is based on slopes that failed, it reflects the maximum possible RSS, a worst-case scenario. By regionalizing this model, this scenario propagates everywhere and thus overestimates the instability of slopes that might have experienced some RSS but not enough to cause failure. This limitation cannot be overcome unless RSS is estimated in unfailed slopes, a capability beyond our approach. Nevertheless, extrapolating the maximum RSS constitutes a useful experiment. Figure 6 summarizes the numerical aspects of the model: the dominant covariate is LR (mean $\beta_{LR}$ = −2.62), followed by PGA (mean $\beta_{PGA}$ = 1.89) and TPI (mean $\beta_{TPI}$ = 0.19). All variables are significant (i.e., the distribution of regression coefficients does not intersect the zero line, Fig. 6a), which also is confirmed by $p$-values < 0.001 calculated for LR, PGA, and TPI.

The sign and the absolute value of the regression coefficients indicate the role of each covariate. Our findings show that LR is strongly negative, PGA is strongly positive, and TPI is slightly positive. We interpret these findings in the discussion section.

The model fits the data well, as shown by the clustering of observed and predicted RSS values along a 45° line (Fig. 6b). This is maintained from low to high quantiles, with the exception of very large observed RSS values, which are slightly underestimated (as shown via the probability density function (PDF) of the residuals, centered at zero and with few very positive cases). The deviation from the fitted model for RSS values of >70% might be due to the range of RSS values in the target dataset. Figure 5 shows that a
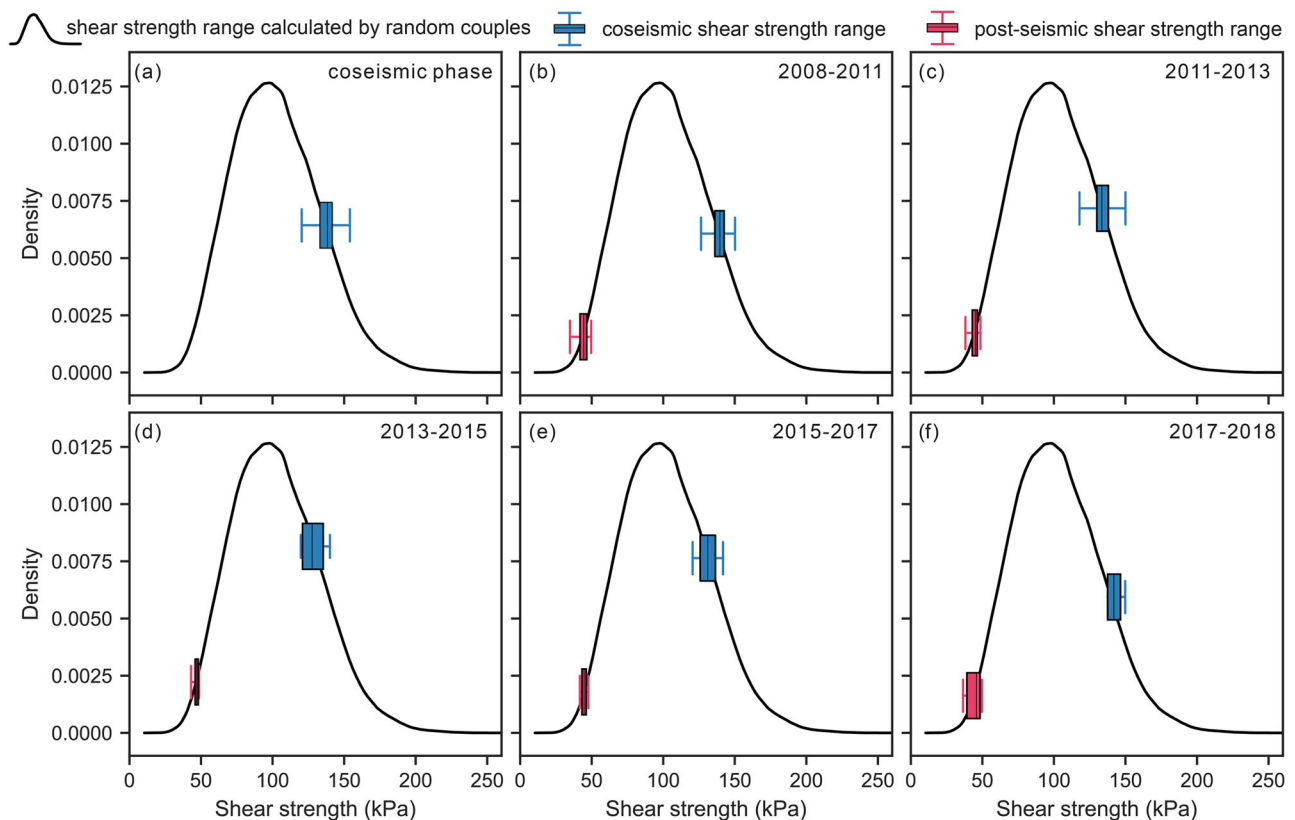
**Fig. 3 | An example for 3-m-thick landslides on granite slope showing the shear-strength range in each time window.** The black curves are the shear strength calculated by random cohesion and friction-angle couples built based on the Gaussian distribution. The horizontal boxplots are selected shear-strength ranges fulfilling unfailed hillslopes in coseismic (blue boxplots) and failed hillslopes in post-seismic phases (red boxplots). The panels show the shear strength range for each time windows of (**a**) coseismic phase, (**b**) 2008–2011, (**c**) 2011–2013, (**d**) 2013–2015, (**e**) 2015–2017, (**f**) 2017–2018. Supplementary Fig. 2 shows similar plots for other lithologic units and landslide thicknesses.

large number of our landslides have RSS values ranging between ~65% and ~70%.

Applying a predictive equation spatially requires assessing both the goodness of fit and the predictive performance of the data-driven model. Therefore, we include random cross-validation with a 90/10 split, iterated 100 times. Results are shown in Fig. 6c, d, with very high values of the Pearson Correlation Coefficient (PCC, centered at 0.81) associated with very low values of Mean Absolute Error (MAE). Notably, the PCC distribution appears to be positively skewed, implying that in most of the 100 cross-validation replicates, the prediction is better than what is shown through the mean.

Having shown that our RSS prediction is reliable both for interpretation and performance, we produce a predictive equation for the entire study area (Fig. 7). RSS increases from northwest to southeast. As would be intuitively expected, it is thus greatest near the fault, where ground shaking was the most intense.

## Discussion
Geotechnical characterization of hillslope materials is by far the greatest challenge for physically based models. Most regions of the world lack available high-quality shear-strength data. Perhaps more challenging is the inherent spatial variability in the physical properties of mapped geologic units and consequent difficulty in characterizing rock-mass properties at regional scale[7,34,35]. For bedrock slopes, overall rock-mass strength is governed more by pre-existing discontinuities (faults, joints, bedding planes, etc.) than by the strength of intact material such as might be sampled and tested in the laboratory. The shape and dimensions of bedrock landslides commonly are defined by the presence, orientation, and spacing of such discontinuities[35,57,58]. And in both rock and soil, mapped geologic units

generally include layers of widely differing strength properties, which makes assigning a single strength to a unit inherently uncertain[14]. In spite of these difficulties, laboratory-based cohesion and friction-angle couples are used widely at regional scale in physically based slope stability analyses[15,59,60]. Selection of cohesion and friction-angle couples is a source of uncertainty in these and other mechanistic approaches.

Our study aims to minimize the uncertainties detailed above by combining multiple approaches. First, we apply back-analyses for all multi-temporal landslide inventories. This means that we identify cohesion and friction-angle couples fulfilling stability and failure conditions in coseismic and post-seismic phases, respectively, though the initial shear-strength parameters are material properties taken from the literature. We then build theoretical Gaussian distributions around these mean values to simulate a wider range of values to model the instability conditions. To minimize or unfold various source of uncertainties regarding parameter selection, we replicate our analyses for a range of values for additional parameters. For example, we test a wide range of COV values to identify the most suitable Gaussian distribution that cohesion and friction-angle values could follow. We should stress that although shear strength parameters generally follow a normal distribution[61–63], this assumption may not hold everywhere. Therefore, upon acquisition of site-specific geotechnical analyses that would yield skewed distributions of shear-strength parameters, these would need to be addressed accordingly. In other words, one would need to fit a suitable distribution to the data and simulate from there. However, in the context of the analyses presented here, such information is not available.

Also, we replicate our analyses for different landslide thicknesses to assess the associated sensitivity in the RSS estimates. We run this sensitivity test for landslide thicknesses ranging between 2 m and 5 m. Where landslide thickness is <2 m or >5 m, the given range of shear strength will not fulfill the
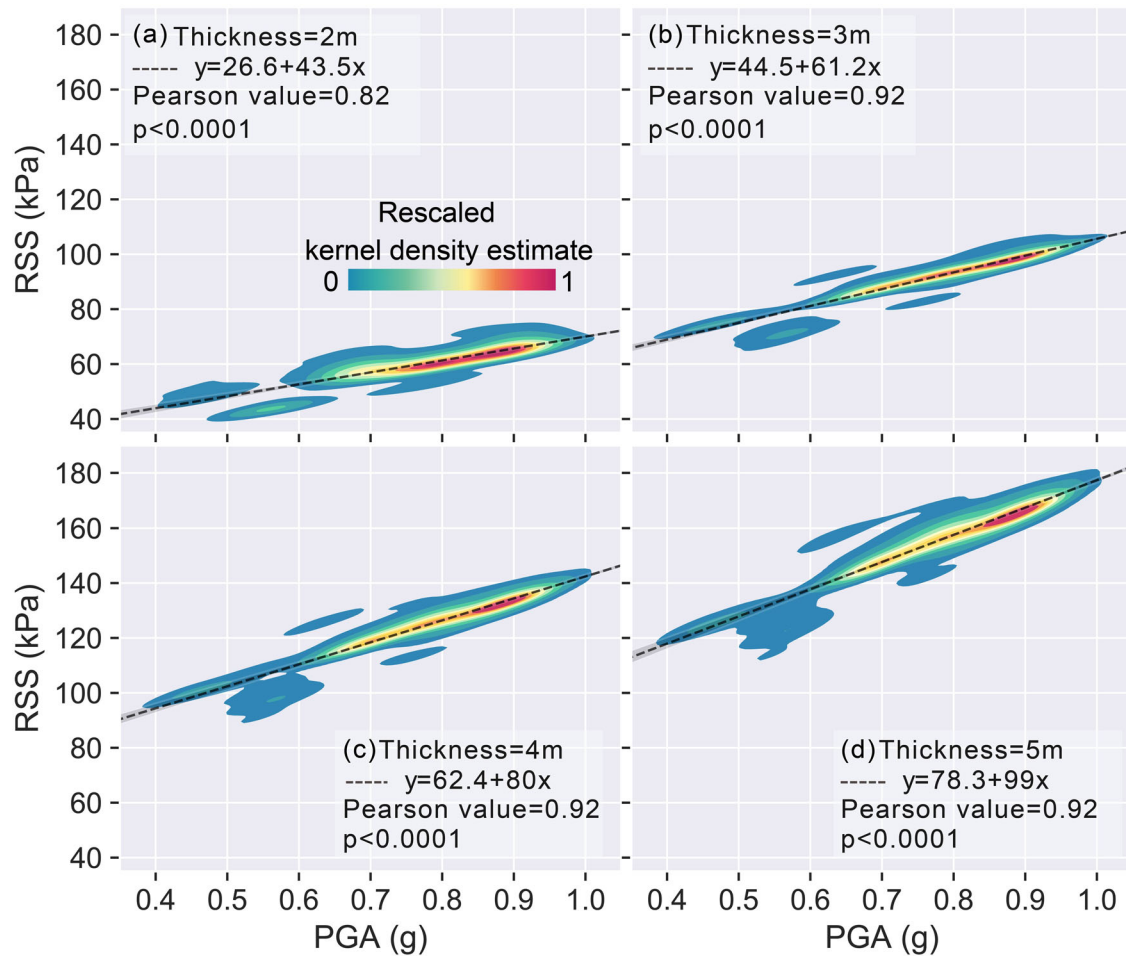
**Fig. 4 | Reduction in shear strength (RSS) in response to range of PGA values.** RSS generated for landslide thicknesses of (**a**) 2 m, (**b**) 3 m, (**c**) 4 m, and (**d**) 5 m. Gray shaded area indicates the 99% confidence interval.

failure condition in the post-seismic phase; thus, we do not expand the sensitivity test for those shallower and deeper landslides. Despite this limitation, the performed test still demonstrates the influence of landslide thickness in RSS calculations.

Second, we complement this approach by calculating the difference in shear strength corresponding to stable and unstable conditions, which we express as a percentage. In a regional analysis, strength differences between units are more important than highly accurate strength estimations for each unit[15]. This certainly is true in our analysis, and in a similar sense, the RSS is of greater interest than the absolute strength. Therefore, targeting not the actual shear strength but the required reduction of them by testing a range of possible cohesion and friction-angle couples, as well as landslide thicknesses, is a way to minimize uncertainty.

Other approaches to capture the uncertainty in model inputs have been suggested, the most common of which is logic trees, wherein estimates of the upper, lower, and most likely values of input parameters are estimated, and weights are assigned to each value for model iteration[51,64]. These approaches are simple to use and intuitive, but choosing weighting factors can be subjective and difficult to rationalize[65].

Our approach does not completely remove the uncertainties described above because it is based on several simplifications. Hillslopes do not necessarily even experience a weakening effect after an earthquake; they can be strengthened or weakened in post-seismic periods depending on type of hillslope material, hillslope geometry, intensity of ground shaking, and accumulated shear strain along the failure surface[19,20]. Nevertheless, characterizing these parameters requires detailed geotechnical field and laboratory investigations, which is practical for regional-scale analyses.

Ideally, we would segregate the analysis based on different types of landslides. Also, focusing on landslide source areas rather than entire landslide areas would yield more accurate results. Unfortunately, the landslide inventories analyzed make no such distinctions.

Another simplification is expressing ground shaking using only PGA provided by empirical equations. Although this ignores site effects, frequency content, and duration of shaking[66], it is a widely used approach in regional-scale slope-stability assessments[14,41] because numerical earthquake simulations of these parameters over broad regions are both uncommon and time consuming[67,68].

Also, we use $m$, a value representing the proportion of a landslide block that is saturated in response to the extreme rainfall events, because identifying the absolute groundwater level at regional scale is impossible. However, $m$ could also be assigned, for instance, considering average or cumulative precipitation for a given period[69]. Therefore, in the Method section, we provide sensitivity analysis on RSS depending on the $m$ value.

Our findings show that RSS has a strong positive correlation with landslide thickness and that variation in RSS can be expected at different landslide depths (see Fig. 4). To further explore this variation, we examine the converted RSS values in percentages and observe consistent results, though depth differences are far less pronounced than for the absolute values and converge at higher ground motions (see Fig. 5). One possible reason for the depth-dependence of RSS is that coseismic slope damage occurs at several scales, from weakening interparticle cohesion to fracturing slope material at centimeter to meter scale. Thus, deeper slides characterized by larger volumes would accumulate slope damage across all scales, and shallow slides are likely to have proportionally less damage.
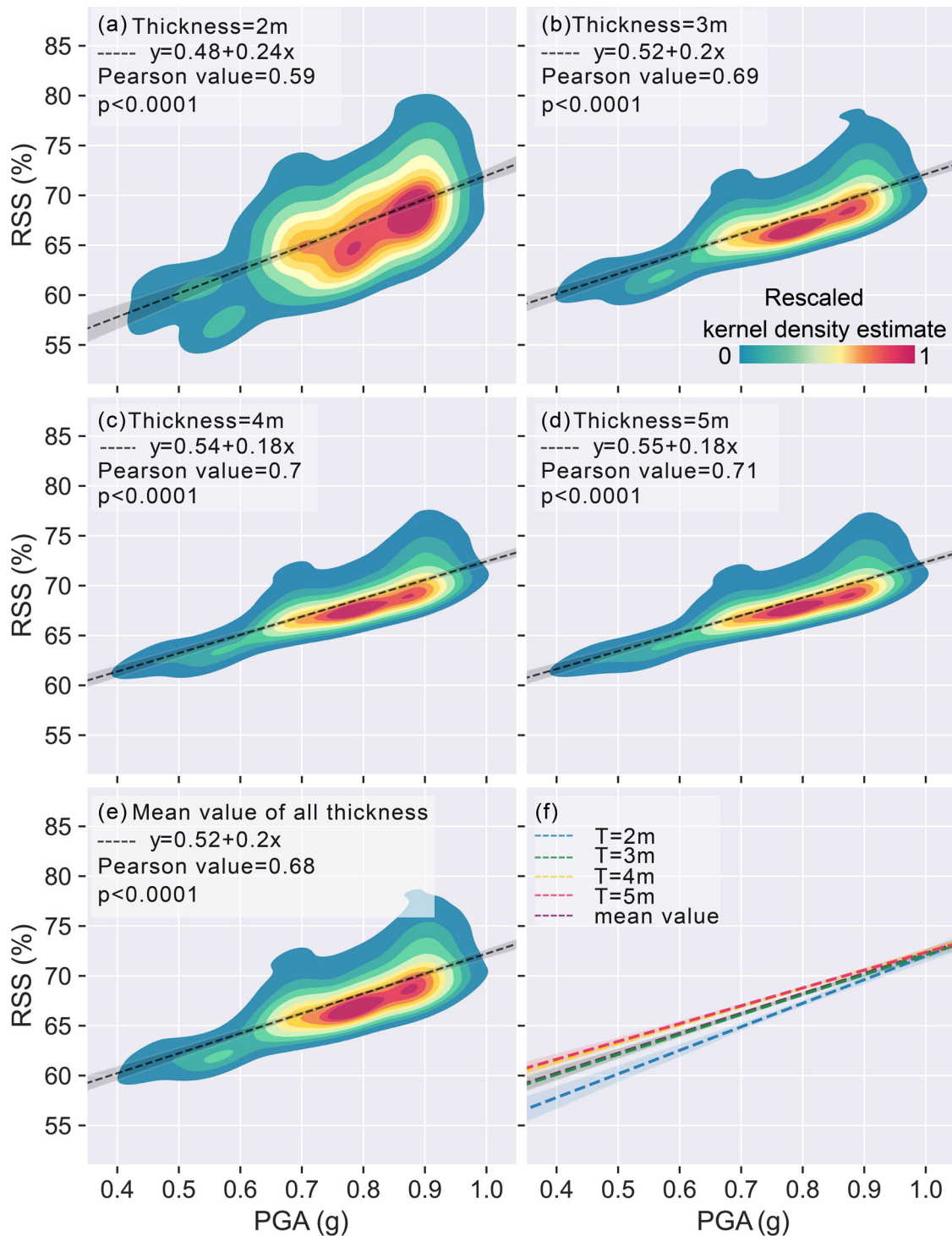
**Fig. 5 | Reduction in shear strength (RSS) expressed as percentages for landslide thicknesses.** RSS generated for landslide thicknesses of (**a**) 2 m, (**b**) 3 m, (**c**) 4 m, (**d**) 5 m. Panel (**e**) shows mean values estimated from all landslide thicknesses, and panel (**f**) shows best linear fits provided for all thicknesses. Gray shaded area indicates the 99% confidence interval.

Overall, our analyses show that near-surface rock strength can be reduced as much as 75% if a hillslope experiences ground shaking >0.9 g. Although this is the maximum theoretical strength reduction, it still is a dramatic hillslope weakening process.

We extrapolate our approach to parts of the study area unaffected by mapped landslides by building a data-driven model. We apply the calculated RSS values to the rest of the study area and then interpret the role of our predictive variables based on regression coefficients. LR is anti-correlated

with RSS. Greater values of LR correspond to large local variations in elevation, and thus this it is generally correlated with stronger rocks, which are more resistant to erosion by frost cracking or landsliding[70]. As for PGA, higher shaking levels could damage both unconsolidated and consolidated materials, though perhaps not to the same extent. Most unconsolidated materials have some cohesion, which would likely be reduced or eliminated by strong shaking. More consolidated materials would likewise undergo reduction in cohesion and possible fracture formation. However, we lack
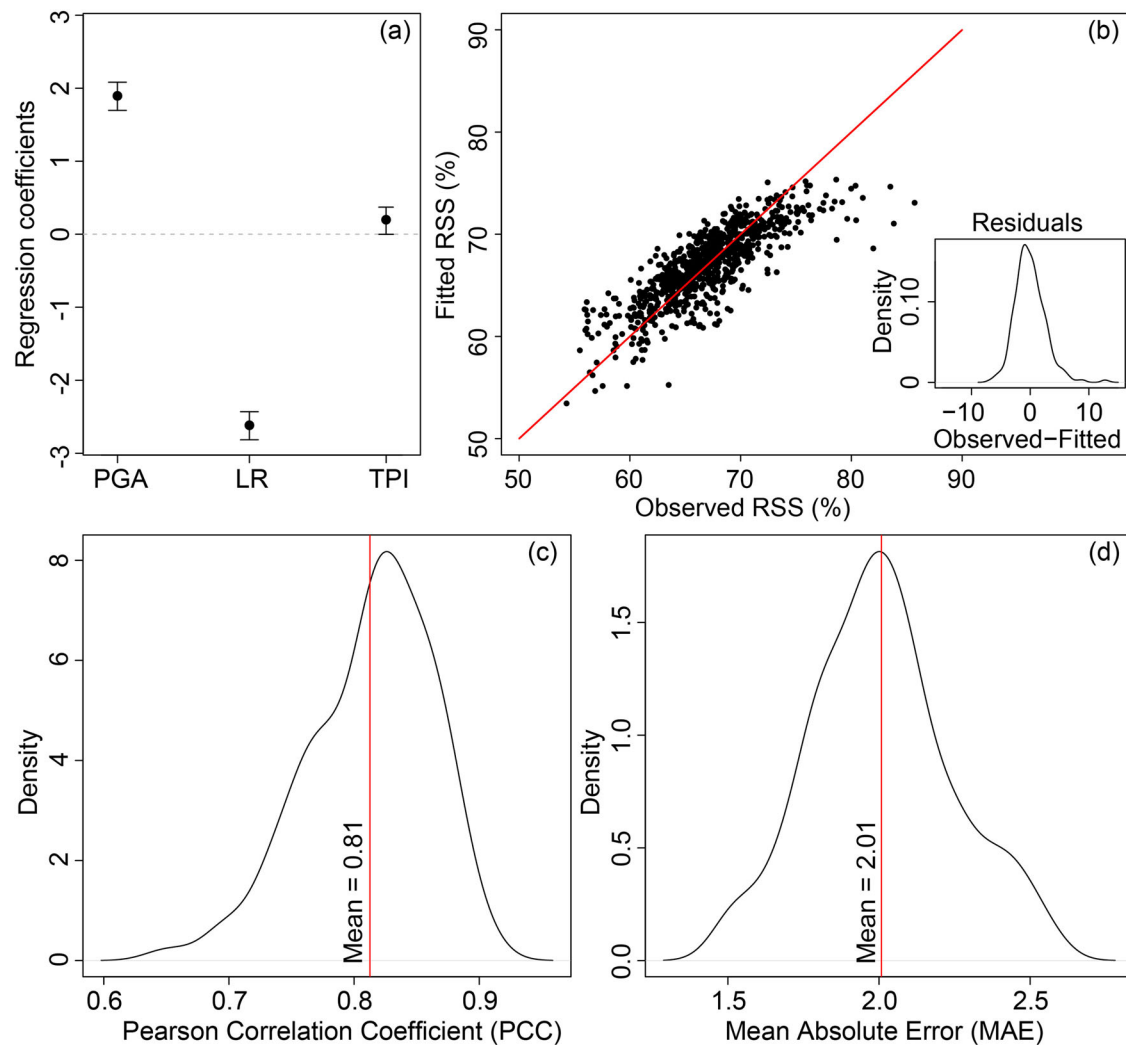
Fig. 6 | Outputs of the data-driven model (Gaussian GLM). a Regression coefficients. b Observed versus fitted values with residuals. c Pearson Correlation Coefficient (PCC). d Mean Absolute Error (MAE) of the validation results.

sufficient observations in each lithologic unit in post-seismic landslide locations to derive a statistically sound conclusion. Therefore, further analyses are required to test the transferability of our approach to other landscapes. Also, the RSS of different lithologic units requires further examination. In this context, multi-temporal landslide inventories generated for other earthquake-affected areas[12] and, in particular, inventories representing the temporal variations in spatial distributions of landslides[71] are primary targets to test the transferability of the proposed approach. RSS would be different for reactivated versus new landslides. Also, landslide polygons separately generated for source and runout areas would provide better insight into RSS because the source is the main area needs to be taken into account while checking slope stability. However, landslide inventories rarely differentiate source areas from runouts[72,73].

The marked increase in RSS with proximity to the fault zone (see Fig. 7) shows the dominant role of seismic ground motion in weakening slope materials. In the near-fault area, static strain induced by fault movement also can weaken near-surface material[74]. The combined effects of fault-driven near-surface deformation and extreme ground shaking make this zone near the fault particularly susceptible to RSS and consequent slope failure. However, these aspects also require further investigations and seismic surveys, which have been used to assess hillslope strength[39,75].

The ideal validation of our modeling approach would require a field survey to measure hillslope material strengths in both pre-seismic and post-seismic periods. Such data collection generally is unfeasible, and we

know of no cases where it has been done. In a few instances, pre-existing geotechnical data have been compiled after a major earthquake to facilitate modeling slope conditions at the time of the seismic shaking. For example, after the Northridge, California (USA) earthquake in 1994[76], Jibson et al.[15] compiled pre-existing geotechnical data across the region to model pre-seismic slope conditions. A program to sample and test a statistically significant number of samples in the dozens of geologic units in the area after the earthquake would have been cost-prohibitive and nearly impossible in practice. Jibson and Michael[59] compiled geotechnical data to construct a seismic landslide hazard map of Anchorage, Alaska (USA), which provided needed pre-seismic data when the 2018 Anchorage earthquake occurred[77]. Again, though, collecting and testing large numbers of soil and rock samples following the earthquake could not reasonably be undertaken. Pre-seismic geotechnical data generally come from local government repositories that contain reports from private consultants who perform laboratory shear-strength testing for building projects. Such repositories can contain hundreds or thousands of geotechnical reports that accumulate over years to decades and thus have a statistically robust amount of data in different geologic units in many locations. Any attempt to replicate such a dataset after an earthquake would be impossible. Also, the coseismic damage to slope materials occurs at landscape scale; collecting samples small enough for geotechnical testing would miss the larger extent of the coseismic disturbance. This is the main justification for our experimental design. At
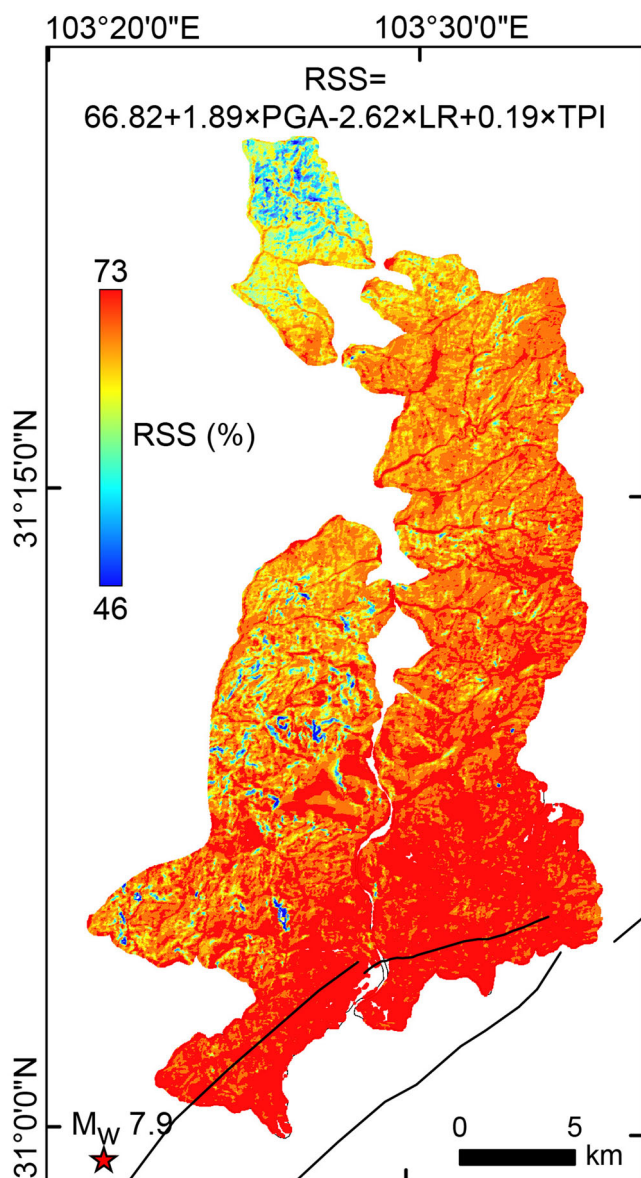
**Fig. 7 | Spatial distribution of estimated RSS based on the fitted model.** The red star indicates the epicenter of the Wenchuan earthquake; black lines show the coseismic surface rupture. The equation shown above corresponds to the linear combination of each model component.

present the only approach we know of to estimate coseismic RSS is back-analysis, and we offer one approach to this. This may prove to be useful in other seismically active areas, albeit more experiments are required to explore its portability, reliability, and consistency, especially for different earthquake magnitudes, geologic settings, and terrain complexities.

## Methods
### Inputs
The multi-temporal landslide inventories associated with the 2008 Wenchuan earthquake were mapped mainly based on high-resolution (SPOT-5 and 6, Worldview-2, Pleiades) satellite imagery[43]. The dataset provides polygons of remobilized and new landslides.

Source and runout areas of landslides were not differentiated in the dataset; thus, to estimate representative topographic, seismic, and meteorological variables for each landslide, we determine the highest elevation point in each polygon. For those points, we extract the corresponding factors for both back-analysis and developing the data-driven model. Specifically,

for the back-analyses we identify the main environmental and triggering conditions controlling the slope stability, including lithology, slope steepness, ground shaking, and rainfall. We use NASA's (earthdata.nasa.gov) DEM (12.5 m spatial resolution) for topography, the U.S. Geological Survey (USGS) ShakeMap of the 2008 Wenchuan earthquake[78] for PGA (~1 km spatial resolution), and rainfall data from the Climate Hazards Group InfraRed Precipitation with Station (CHIRPS, ~5 km spatial resolution). Lithologic descriptions are taken from the National Geological Data Library of China Geological Survey (http://www.ngac.org.cn). As for the data-driven model, we use PGA, LR, and TPI.

### Estimating reduction in shear strength
We follow a four-step methodology: (1) pre-processing, (2) back-analysis, (3) estimating the RSS, and (4) extrapolating the estimated RSS via a data-driven model (Fig. 8).

### Step-1
Step-1 involves pre-processing the data. We gather cohesion and friction angles (Table 1) proposed in the literature for the lithologic units we have in our study area. We use these couples later on to estimate shear strength of hillslope materials. We assume that effective shear-strength ($\tau'$) parameters follow the Mohr-Coulomb failure criterion:

$$\tau' = \sigma' \tan \varphi' + c' \tag{1}$$

where $\varphi'$ is the effective internal friction angle, $c'$ is the effective cohesion, and $\sigma'$ is effective normal stress, which can be expressed as:

$$\sigma' = (\gamma t - \gamma_w tm) \cos \alpha \tag{2}$$

where $\gamma$ is the unit weight of the soil/rock material, $\gamma_w$ is the unit weight of water, $\alpha$ is the slope angle (°), $t$ is the landslide thickness, and $m$ is the proportion of the landslide block that is saturated. Thus, $m = 0$ refers to dry conditions, whereas $m = 1$ indicates fully saturated conditions.

### Step-2
In this step, we back-analyze the slopes to identify cohesion and friction-angle couples fulfilling the stability or failure conditions based on a set of assumptions for coseismic and post-seismic periods, defined below.

### Coseismic conditions
For coseismic conditions, we estimate the shear strength ($\tau'_{co}$) of hillslope materials, where post-seismic landslides are stable during the earthquake, using two assumptions: (1) hillslope materials are dry and (2) the hillslope remains stable if the critical acceleration ($a_c$) is greater than the estimated PGA at any given location[79]. We check the first assumption by calculating the standard precipitation index (SPI)[80], a widely used index expressing the droughtiness of an examined period for a given location[81,82]. We calculate SPI for our study area for the month of the earthquake (May 2008) and for the two prior months using the 10-year CHRPS daily precipitation dataset between 2008 and 2017. SPI values for those periods are −1.09 (moderately dry) and −1.58 (severely dry), respectively. Based on these findings, we assume that the contribution of precipitation to landsliding was negligible during the coseismic event.

As for the second assumption, we characterize seismic slope stability based on the Newmark approach[79], which models the sliding mass as a rigid block on an inclined plane. The block has a known critical acceleration, the seismic acceleration required to overcome basal shear resistance and initiate permanent downslope displacement. The critical acceleration can be approximated accurately as follows:

$$a_c = (FS - 1)g \sin \alpha \tag{3}$$

where $FS$ is the static factor of safety, $g$ is the acceleration of gravity (9.81 m/s²), and $\alpha$ is the slope angle[79]. A further simplification generally
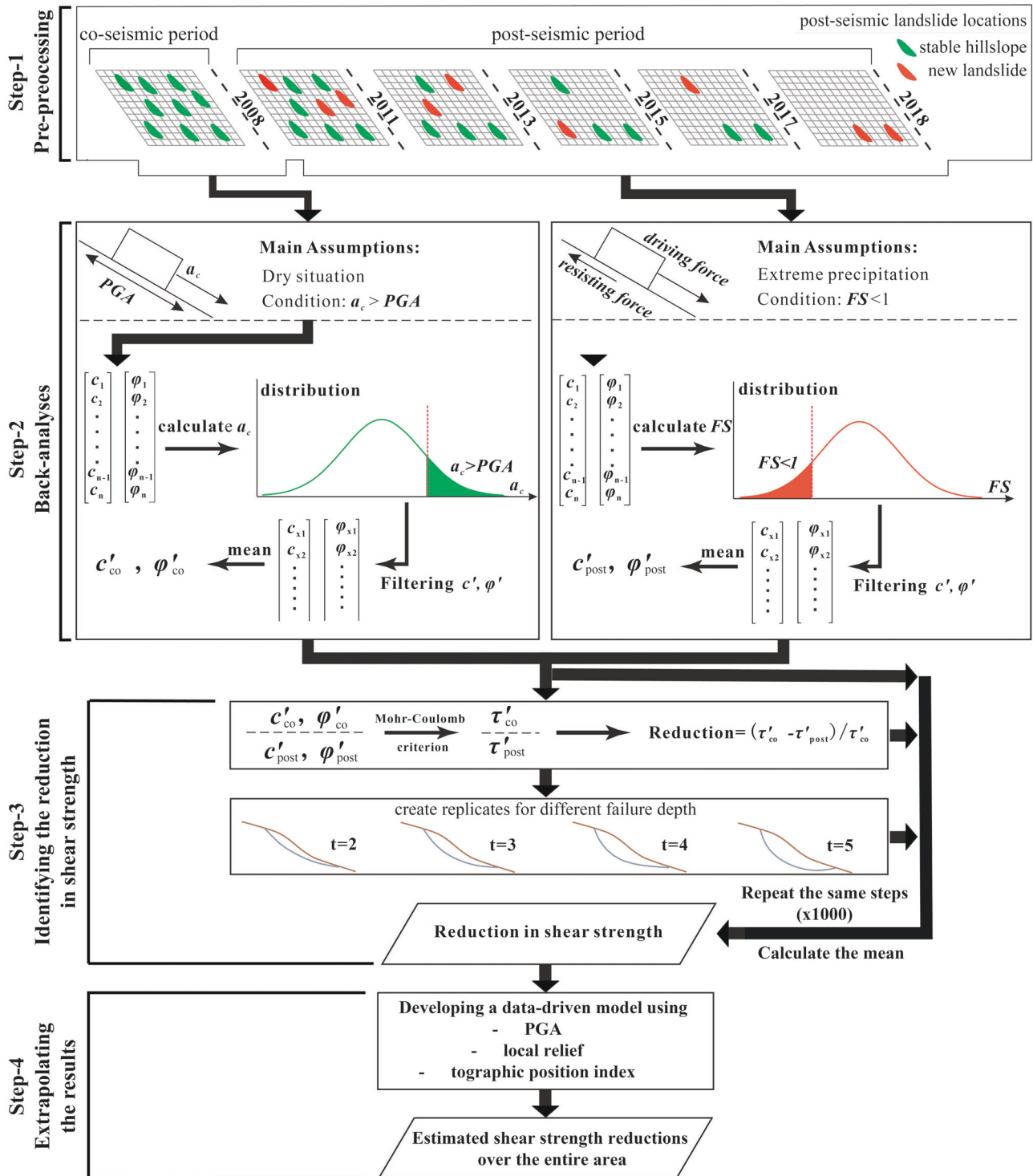
**Fig. 8 | Flowchart for identifying the reduction in effective shear strength (RSS).** $c'_{co}$ and $\varphi'_{co}$ are cohesion and friction angle of post-seismic landslide locations during the earthquake where they were still stable. $c'_{post}$ and $\varphi'_{post}$ refer to their post-seismic counterparts representing the failure condition.

applied is that landslides are infinite-slope failures, which allows calculation of *FS* as follows:

$$FS = \frac{c'}{\gamma t \sin \alpha} + \frac{\tan \varphi'}{\tan \alpha} - \frac{m \gamma_w \tan \varphi'}{\gamma \tan \alpha} \quad (4)$$

in which the first term accounts for the cohesive component of the shear strength, the second term for the frictional strength, and the third

term for the reduction in frictional strength due to pore-water pressure[15].

## Post-seismic periods
We quantify the post-seismic shear strength ($\tau'_{post}$) analogously to the coseismic situation by assuming that the post-seismic landslides were triggered by extreme rainfall events. We use a range of *m* values representing the groundwater response to the extreme rainfall events recorded during the

examined time windows[69]. We calculate the mean of extreme daily precipitation (above 95th percentile) in each grid for each post-seismic period (Supplementary Fig. 3); then, we assign $m$ values to each grid by rescaling the calculated extreme precipitation values between 0 and 1. Failure is assumed to have occurred in cells where $FS < 1$. This approach is consistent with other studies where precipitation is used to diminish the influence of meteorologic effects from post-seismic landsliding and to isolate the role of earthquake legacy effect[28].

Based on this approach, we also quantify the influence of $m$ in the calculation of RSS for the coseismic phase, which we assume it is dry. Despite this assumption, supported by SPI, we also run our analyses for a hypothetical fully saturated condition, where $m = 1$. The result shows a maximum uncertainty of 3.36% in RSS caused by groundwater level (Supplementary Fig. 4).

## Back-analyses

We first test the role of two variables capable of influencing the slope-stability model: landslide thickness and the coefficient of variation ($COV$) of distributions of cohesion and friction-angle pairs.

For each landslide thickness, we randomly create shear-strength parameters using a Monte Carlo simulation, a commonly used approach for addressing the uncertainty of soil and rock properties in engineering geological problems[63,83,84]. To run the simulations, we estimate the distribution of shear-strength parameters. Ranges of cohesion and friction angle for a given rock or soil unit commonly are represented using a Gaussian distribution[61-63]. However, the shape of the distribution needs to be identified because different variances around the mean can lead to large simulation differences. Therefore, we test different $COV$ values, calculated as the standard deviation divided by the mean, to control the



**Fig. 9 | Variation in COV values with respect to True Negative Rate (TNR).** Panels showing (**a**) map of estimated TP, FN, and TN, (**b**) cohesion distribution of granite using different $COV$s, and (**c**) variation between cohesion $COV$s and TNR for different landslide thicknesses.
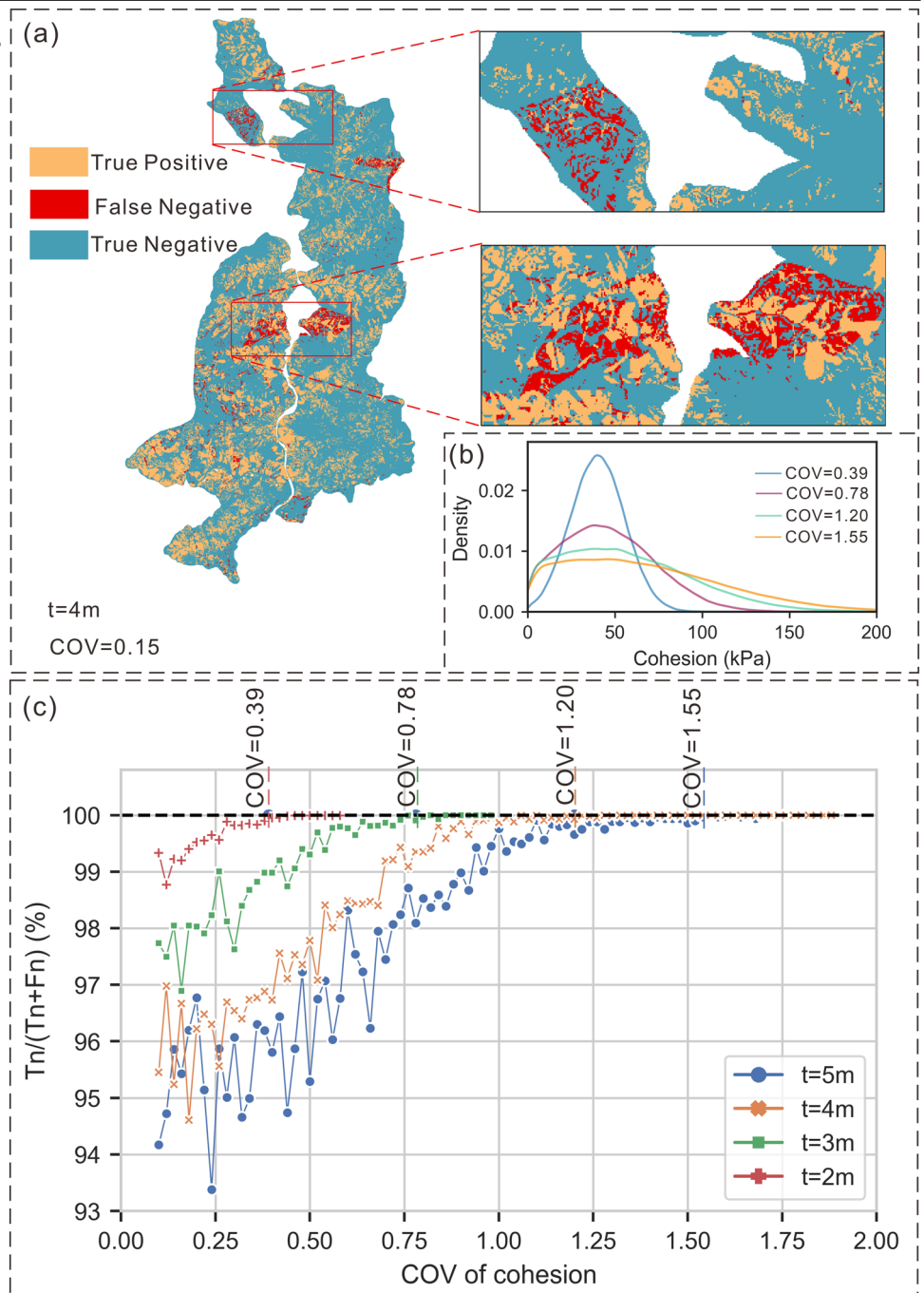
width of the Gaussian distribution. Because we assume both cohesion and friction angle follow the Gaussian distribution, while testing *COV* values for one of these shear-strength parameters, we keep the other constant. Following Phoon and Kulhawy[85], we set the *COV* of friction angle at 0.15. For cohesion, we assign different *COVs* for different landslide thicknesses. This step does not involve back-analysis, but rather the direct solution of the Newmark method for the coseismic landslide inventory. We use the cohesion and friction-angle couples suggested in the literature as the beginning means (Table 1) and then build theoretical Gaussian distributions around these mean values for each rock unit (Fig. 1). This allows estimation of the *COVs* that best match the unfailed hillslopes.

To numerically identify the best match, we target unfailed hillslopes during the co-seismic phase. For those stable hillslopes, we test different *COV* values and accordingly generate cohesion and friction-angle couples. Based on those couples, we calculate critical acceleration using Eq. 5. If the given *COV* value of cohesion does not ensure the stability of a given hillslope ($a_c$ < PGA), then we label the hillslope as False Negative (FN); otherwise ($a_c$ < PGA), we label it as True Negative (TN). As a result, we calculate the True Negative Rate (TNR) for all tested *COVs* of cohesion and define the best match as giving highest value (Fig. 9):

$$\text{TNR} = [\text{TN}/(\text{TN} + \text{FN})] \times 100 \qquad (5)$$

These analyses show that *COVs* of 0.39, 0.78, 1.2, and 1.55 give the highest TNRs for thicknesses of 2 m, 3 m, 4 m, and 5 m, respectively. As mentioned above, these values are estimated for a fixed *COV* of friction angle (*COV* = 0.15). However, to assess the uncertainty of using such a fixed value, we also test *COVs* ranging from 0.12 to 0.22. Specifically, for different *COVs* of friction angle, we keep its counterpart for the cohesion and calculate its influence on RSS. This test show that the variations in RSS due to the choice of *COV* is <2.1% (Supplementary Fig. 5).

### Step-3
We run 1,000 Monte-Carlo simulations to repeat all steps summarized above to minimize the error due to a fixed parameter choice and to determine a final result as the mean of 1,000 simulations. In each simulation, we randomly select 5,000 cohesion and friction-angle couples to calculate *FS* and $a_c$. Then, we calculate the RSS between co-seismic ($\tau'_{co}$) and post-seismic ($\tau'_{post}$) phases, represented by actual values ($RSS_v$) and percentages ($RSS_p$):

$$RSS_v = \tau'_{co} - \tau'_{post} \qquad (6)$$

$$RSS_p = \left[ \frac{\left( \tau'_{co} - \tau'_{post} \right)}{\tau'_{co}} \times 100 \right] \qquad (7)$$

Up to this point, the estimated RSSs are generated only for post-seismic landslide locations. However, RSS likely occurred across the entire region. We therefore introduce a final step to regionalize the greatest expected RSS across the study area. To do so, we use a Generalized Linear Model (GLM) where the RSS is the response (dependent) variable, assumed to have a Gaussian distribution. We use three input (independent) variables: (1) Local Relief (LR), the difference in elevation between each grid cell and the mean of all grid-cells within a 100 m radius; (2) Topographic Position Index (TPI[86]), a terrain classification method indicating the relevant position of a given location with respect to its neighborhood; and (3) PGA.

The resulting GLM can be denoted as

$$E(Y) = \beta_0 + \beta_{LR}LR + \beta_{TPI}TPI + \beta_{PGA}PGA \qquad (8)$$

where $E(Y)$ is the expected shear strength reduction (RSS), $\beta_0$ is the global intercept, and $\beta_{LR}, \beta_{TPI}, \beta_{PGA}$ are the regression coefficients estimated for each corresponding covariate.

To verify the functionality of the model, we cross-validate by sampling, without replacement, 100 times the data, and extracting a subset made of 90% of the data for calibration and 10% for validation. At each iteration, we store the Pearson Correlation Coefficient (PCC) and the Mean Absolute Error (MAE).

### Data availability
Multi-temporal landslide inventories generated by Fan et al. (2019) are available through the following link: https://zenodo.org/records/1484667. The ShakeMap form U.S. Geological Survey (USGS) is available through the following link: https://www.usgs.gov/. The rainfall data from the Climate Hazards Group InfraRed Precipitation with Station Data is also available through the following link: https://developers.google.com/earth-engine/datasets/catalog/UCSB-CHG_CHIRPS_DAILY. Geologic map is taken from National Geological Data Library of China Geological Survey: http://www.ngac.org.cn/Map/Document?guid=EC7E1A7A78DA1954E043010 0007F182E. All other dataset used in the manuscript are available through the following link: https://zenodo.org/records/10302609.

### Code availability
The source code used in the analyses is available through the following link: https://zenodo.org/records/10302609.

### References
1. Nadim, F., Kjekstad, O., Peduzzi, P., Herold, C. & Jaedicke, C. Global landslide and avalanche hotspots. *Landslides* **3**, 159–173 (2006).
2. Budimir, M. E. A., Atkinson, P. M. & Lewis, H. G. A systematic review of landslide probability mapping using logistic regression. *Landslides* **12**, 419–436 (2015).
3. Crozier, M. J. & Glade, T. Landslide hazard and risk: issues, concepts and approach. *Landslide Hazard Risk* https://doi.org/10.1002/9780470012659.ch1 (2005).
4. Fell, R. et al. Guidelines for landslide susceptibility, hazard and risk zoning for land use planning. *Eng. Geol.* **102**, 85–98 (2008).
5. Korup, O. et al. Giant landslides, topography, and erosion. *Earth Planet. Sci. Lett.* **261**, 578–589 (2007).
6. Korup, O. Linking landslides, hillslope erosion, and landscape evolution. *Earth Surf. Process. Landforms* **34**, 1315–1317 (2009).
7. Larsen, I. J. & Montgomery, D. R. Landslide erosion coupled to tectonics and river incision. *Nat. Geosci.* **5**, 468–473 (2012).
8. Hovius, N. & Stark, C. P. *Landslide-Driven Erosion and Topographic Evolution of Active Mountain Belts* (Springer, 2006).
9. Densmore, A. L., Anderson, R. S., McAdoo, B. G. & Ellis, M. A. Hillslope evolution by bedrock landslides. *Science* **275**, 369–372 (1997).
10. Nowicki Jessee, M. A. et al. A global empirical model for near-real-time assessment of seismically induced landslides. *J. Geophys. Res. Earth Surf.* **123**, 1835–1859 (2018).
11. Stanley, T. A. et al. Data-driven landslide nowcasting at the global scale. *Front. Earth Sci.* https://doi.org/10.3389/feart.2021.640043 (2021).
12. Tanyaş, H., Kirschbaum, D. & Lombardo, L. Capturing the footprints of ground motion in the spatial distribution of rainfall-induced landslides. *Bull. Eng. Geol. Environ.* **80**, 4323–4345 (2021).
13. van Westen, C. J., Castellanos, E. & Kuriakose, S. L. Spatial data for landslide susceptibility, hazard, and vulnerability assessment: an overview. *Eng. Geol.* **102**, 112–131 (2008).
14. Dreyfus, D., Rathje, E. M. & Jibson, R. W. The influence of different simplified sliding-block models and input parameters on regional

predictions of seismic landslides triggered by the Northridge earthquake. *Eng. Geol.* **163**, 41–54 (2013).

15. Jibson, R. W., Harp, E. L. & Michael, J. A. A method for producing digital probabilistic seismic landslide hazard maps. *Eng. Geol.* **58**, 271–289 (2000).

16. Gallen, S. F., Clark, M. K., Godt, J. W., Roback, K. & Niemi, N. A. Application and evaluation of a rapid response earthquake-triggered landslide model to the 25 April 2015 Mw 7.8 Gorkha earthquake, Nepal. *Tectonophysics* **714–715**, 173–187 (2017).

17. Kim, D., Im, S., Lee, S. H., Hong, Y. & Cha, K.-S. Predicting the rainfall-triggered landslides in a forested mountain region using TRIGRS model. *J. Mt. Sci.* **7**, 83–91 (2010).

18. Mergili, M., Fischer, J.-T., Krenn, J. & Pudasaini, S. P. r. avaflow v1, an advanced open-source computational framework for the propagation and interaction of two-phase mass flows. *Geosci. Model Dev.* **10**, 553–569 (2017).

19. Brain, M. J., Rosser, N. J. & Tunstall, N. The control of earthquake sequences on hillslope stability. *Geophys. Res. Lett.* **44**, 865–872 (2017).

20. Brain, M. J. et al. Controls on post-seismic landslide behavior in brittle rocks. *J. Geophys. Res. Earth Surf.* **126**, e2021JF006242 (2021).

21. Yang, Z. et al. Unsaturated hydro-mechanical behaviour of rainfall-induced mass remobilization in post-earthquake landslides. *Eng. Geol.* **222**, 102–110 (2017).

22. Leshchinsky, B., Lehmann, P. & Or, D. Enhanced rainfall-induced shallow landslide activity following seismic disturbance—from triggering to healing. *J. Geophys. Res. Earth Surf.* **126**, e2020JF005669 (2021).

23. Lin, C.-W. et al. Impact of Chi-Chi earthquake on the occurrence of landslides and debris flows: example from the Chenyulan River watershed, Nantou, Taiwan. *Eng. Geol.* **71**, 49–61 (2004).

24. Yunus, A. P. et al. Decadal vegetation succession from MODIS reveals the spatio-temporal evolution of post-seismic landsliding after the 2008 Wenchuan earthquake. *Remote Sens. Environ.* **236**, 111476 (2020).

25. Chen, M. et al. The long-term evolution of landslide activity near the epicentral area of the 2008 Wenchuan earthquake in China. *Geomorphology* **367**, 107317 (2020).

26. Tian, Y. et al. Landslide development within 3 years after the 2015 Mw 7.8 Gorkha earthquake, Nepal. *Landslides* **17**, 1251–1267 (2020).

27. Kincey, M. et al. Evolution of coseismic and post-seismic landsliding after the 2015 Mw 7.8 Gorkha earthquake, Nepal. *ESSOAr* https://doi.org/10.1002/essoar.10505237.1 (2020).

28. Marc, O., Hovius, N., Meunier, P., Uchida, T. & Hayashi, S. Transient changes of landslide rates after earthquakes. *Geology* **43**, 883–886 (2015).

29. Tanyaş, H. et al. A closer look at factors governing landslide recovery time in post-seismic periods. *Geomorphology* **391**, 107912 (2021).

30. Kincey, M. E. et al. Evolution of coseismic and post-seismic landsliding after the 2015 Mw 7.8 Gorkha earthquake, Nepal. *J. Geophys. Res. Earth Surf.* **n/a**, e2020JF005803 (2021).

31. Wyllie, D. C. & Mah, C. *Rock Slope Engineering* Vol. 568 (CRC Press, 2004).

32. Duncan, J. M., Wright, S. G. & Brandon, T. L. *Soil Strength and Slope Stability* Vol. 336 (John Wiley & Sons, 2014).

33. Heyman, J. *Coulomb's Memoir on Statics: An Essay in the History of Civil Engineering*. https://www.eeri.org/images/archived/wp-content/uploads/USA_CA_NorthPalmSprings_Insert_Sep86.pdfo224 (CUP Archive, 1972).

34. Hoek, E. & Brown, E. T. Empirical strength criterion for rock masses. *J. Geotech. Eng. ASCE* **106**, 1013–1035 (1980).

35. Hoek, E. & Brown, E. T. The Hoek–Brown failure criterion and GSI–2018 edition. *J. Rock Mech. Geotech. Eng* **11**, 445–463 (2019).

36. Barton, N. Review of a new shear-strength criterion for rock joints. *Eng. Geol.* **7**, 287–332 (1973).

37. Barton, N. & Choubey, V. The shear strength of rock joints in theory and practice. *Rock Mech.* **10**, 1–54 (1977).

38. Townsend, K. F., Clark, M. K. & Zekkos, D. Profiles of near-surface rock mass strength across gradients in Burial, Erosion, and Time. *J. Geophys. Res. Earth Surf.* **126**, e2020JF005694 (2021).

39. Medwedeff, W. G., Clark, M. K., Zekkos, D., West, A. J. & Chamlagain, D. Near-surface geomechanical properties and weathering characteristics across a tectonic and climatic gradient in the central Nepal Himalaya. *J. Geophys. Res. Earth Surf.* **127**, e2021JF006240 (2022).

40. Bunn, M., Leshchinsky, B. & Olsen, M. J. Geologic trends in shear strength properties inferred through three-dimensional back analysis of landslide inventories. *J. Geophys. Res. Earth Surf.* **125**, 1–25 (2020).

41. Gallen, S. F., Clark, M. K. & Godt, J. W. Coseismic landslides reveal near-surface rock strength in a high-relief, tectonically active setting. *Geology* **43**, 11–14 (2015).

42. Kallimogiannis, V., Saroglou, C., Zekkos, D. & Papadimitriou, A. Back-analyses of co-seismic landslides in carbonate fault rocks due to the Mw 6.5 earthquake (2015) in Lefkada island, Greece. *Eng. Geol.* **309**, 106850 (2022).

43. Fan, X. et al. Two multi-temporal datasets that track the enhanced landsliding after the 2008 Wenchuan earthquake. *Earth Syst. Sci. Data* **11**, 35–55 (2019).

44. Xu, C., Xu, X., Yao, X. & Dai, F. Three (nearly) complete inventories of landslides triggered by the May 12, 2008 Wenchuan Mw 7.9 earthquake of China and their spatial distribution statistical analysis. *Landslides* **11**, 441–461 (2014).

45. Tang, C., Van Westen, C. J., Tanyas, H. & Jetten, V. G. Analysing post-earthquake landslide activity using multi-temporal landslide inventories near the epicentral area of the 2008 Wenchuan earthquake. *Nat. Hazards Earth Syst. Sci.* **16**, 2641–2655 (2016).

46. Fan, X. et al. Spatio-temporal evolution of mass wasting after the 2008 Mw 7.9 Wenchuan earthquake revealed by a detailed multi-temporal inventory. *Landslides* **15**, 2325–2341 (2018).

47. Xu, X. et al. Coseismic reverse- and oblique-slip surface faulting generated by the 2008 Mw 7.9 Wenchuan earthquake, China. *Geology* **37**, 515–518 (2009).

48. Domènech, G. et al. *Two Multi-Temporal Datasets to Track the Enhanced Landsliding after the 2008 Wenchuan Earthquake* (Zenodo, 2018).

49. Parker, R. N. et al. Mass wasting triggered by the 2008 Wenchuan earthquake is greater than orogenic growth. *Nat. Geosci.* **4**, 449–452 (2011).

50. Tang, C. et al. Analysing post-earthquake mass movement volume dynamics with multi-source DEMs. *Eng. Geol.* **248**, 89–101 (2019).

51. Wang, Y. & Rathje, E. M. Probabilistic seismic landslide hazard maps including epistemic uncertainty. *Eng. Geol.* **196**, 313–324 (2015).

52. Yue, X., Wu, S., Yin, Y., Gao, J. & Zheng, J. Risk identification of seismic landslides by joint Newmark and rockfall analyst Models: a case study of roads affected by the Jiuzhaigou earthquake. *Int. J. Disaster Risk Sci.* **9**, 392–406 (2018).

53. Chen, X. L., Liu, C. G., Yu, L. & Lin, C. X. Critical acceleration as a criterion in seismic landslide susceptibility assessment. *Geomorphology* **217**, 15–22 (2014).

54. Xi, C. et al. Effectiveness of Newmark-based sampling strategy for coseismic landslide susceptibility mapping using deep learning, support vector machine, and logistic regression. *Bull. Eng. Geol. Environ.* **81**, 174 (2022).

55. Ma, S. & Xu, C. Applicability of two newmark models in the assessment of coseismic landslide hazard and estimation of slope-failure probability: an example of the 2008 Wenchuan M w 7.9 earthquake affected area. *J. Earth Sci.* **30**, 1020–1030 (2019).

56. Townsend, K. F., Gallen, S. F. & Clark, M. K. Quantifying near-surface rock strength on a regional scale from hillslope stability models. *J. Geophys. Res. Earth Surf.* **125**, e2020JF005665 (2020).

57. Harp, E. L. & Noble, M. A. An engineering rock classification to evaluate seismic rock-fall susceptibility and its application to the wasatch front. *Environ. Eng. Geosci.* **xxx**, 293–319 (1993).

58. Hoek, E. & Brown, E. T. Practical estimates of rock mass strength. *Int. J. Rock Mech. Min. Sci.* **34**, 1165–1186 (1997).

59. Jibson, R. W. & Michael, J. A. *Maps Showing Seismic Landslide Hazards in Anchorage, Alaska.* (US Geological Survey Reston, VA, USA, 2009).

60. Godt, J. et al. Rapid assessment of earthquake-induced landsliding. *Proc. First World Landslide Forum, United Nations Univ. Tokyo* **4**, 3–6 (2008).

61. Nguyen, V. B. Q. & Kim, Y. T. Rainfall-earthquake-induced landslide hazard prediction by monte carlo simulation: a case study of MT. Umyeon in Korea. *KSCE J. Civ. Eng.* **24**, 73–86 (2020).

62. Wolff, T. F., Demsky, E. C., Schauer, J. & Perry, E. *Reliability Assessment of Dike and Levee Embankments*. 636–650 (ASCE, 1996).

63. Xi, C. et al. Predictive model of regional coseismic landslides' permanent displacement considering uncertainty. *Landslides* **19**, 2513–2534 (2022).

64. Wang, Y. & Rathje, E. M. Application of a probabilistic assessment of the permanent seismic displacement of a slope. *J. Geotech. Geoenvironmental Eng.* **144**, 4018034 (2018).

65. Rodríguez-Peces, M. J. et al. Obtaining suitable logic-tree weights for probabilistic earthquake-induced landslide hazard analyses. *Eng. Geol.* **275**, 105743 (2020).

66. Fan, X. et al. Earthquake-induced chains of geologic hazards: patterns, mechanisms, and impacts. *Rev. Geophys*. https://doi.org/10.1029/2018RG000626 (2019).

67. Dahal, A. et al. From ground motion simulations to landslide occurrence prediction. *Geomorphology* **441**, 108898 (2023).

68. Dunham, A. M. et al. Topographic control on ground motions and landslides from the 2015 Gorkha earthquake. *Geophys. Res. Lett.* **49**, e2022GL098582 (2022).

69. Saygili, G. & Rathje, E. M. Probabilistically based seismic landslide hazard maps: an application in southern California. *Eng. Geol.* **109**, 183–194 (2009).

70. Sklar, L. S. & Dietrich, W. E. Sediment and rock strength controls on river incision into bedrock. *Geology* **29**, 1087–1090 (2001).

71. Jones, J., Boulton, S., Bennett, G., Whitworth, M. & Stokes, M. Himalaya mass-wasting: impacts of the monsoon, extreme tectonic and climatic forcing, and road construction. *Copernicus* https://doi.org/10.5194/egusphere-egu2020-8702 (2020).

72. Roback, K. et al. The size, distribution, and mobility of landslides caused by the 2015 Mw7.8 Gorkha earthquake, Nepal. *Geomorphology* **301**, 121–138 (2018).

73. Sato, H. P., Sekiguchi, T., Kojiroi, R., Suzuki, Y. & Iida, M. Overlaying landslides distribution on the earthquake source, geological and topographical data: the mid niigata prefecture earthquake in 2004, Japan. *Landslides* **2**, 143–152 (2005).

74. Morton, D. M. et al. *Ground Fractures and Landslides Produced by the North Palm Springs, California, Earthquake of July 8, 1986. Landslides a Semi-arid Environ.* https://www.eeri.org/images/archived/wp-content/uploads/USA_CA_NorthPalmSprings_Insert_Sep86.pdf (1989).

75. Clarke, B. A. & Burbank, D. W. Bedrock fracturing, threshold hillslopes and limits to the magnitude of bedrock landslides. *Earth Planet. Sci. Lett.* **297**, 577–586 (2010).

76. USGS. *Northridge Earthquake Event Page*. https://earthquake.usgs.gov/earthquakes/eventpage/ci3144585/executive (1994).

77. USGS. *Anchorage Earthquake Event Page* (USGS, 2018).

78. USGS. *United States Geological Survey Earthquake Portal Earthquake Hazards Program*. https://www.usgs.gov/%0Anatural-hazards/earthquake-hazards/earthquakes (2023).

79. Newmark, N. M. Effects of earthquakes on dams and embankments. *Geotechnique* **15**, 139–160 (1965).

80. McKee, T. B., Doesken, N. J. & Kleist, J. The relationship of drought frequency and duration to time scales. In *8th Conference on Applied Climatology* Vol.17, 179–183 (Department of Atmospheric Science, California, 1993).

81. Naresh Kumar, M., Murthy, C. S., Sesha Sai, M. V. R. & Roy, P. S. On the use of standardized precipitation index (SPI) for drought intensity assessment. *Meteorol. Appl. A J. Forecast. Pract. Appl. Train. Tech. Model.* **16**, 381–389 (2009).

82. Svoboda, M., Hayes, M. & Wood, D. *Standardized Precipitation Index: User Guide*. https://library.wmo.int/idurl/4/39629 (2012).

83. Du, W. & Wang, G. Fully probabilistic seismic displacement analysis of spatially distributed slopes using spatially correlated vector intensity measures. *Earthq. Eng. Struct. Dyn.* **43**, 661–679 (2014).

84. Refice, A. & Capolongo, D. Probabilistic modeling of uncertainties in earthquake-induced landslide hazard assessment. *Comput. Geosci.* **28**, 735–749 (2002).

85. Phoon, K. K. & Kulhawy, F. H. Characterization of geotechnical variability. *Can. Geotech. J.* **36**, 612–624 (1999).

86. Weiss, A. *Topographic Position and Landforms Analysis in Poster Presentation* (*ESRI User Conference,* 2001).

## Acknowledgements

## Author contributions

Hakan Tanyas and Chuanjie Xi conceptualized the research idea. Analyses were carried out by Chuanjie Xi, Hakan Tanyas, and Luigi Lombardo. Hakan Tanyas and Chuanjie Xi wrote the first version of the manuscript. Luigi Lombardo and Randall W. Jibson involved in writing of the final version of manuscript, whereas Kun He and Xiewen Hu provided feedback on it.

## Competing interests

The authors declare no competing interests.

## Additional information

**Supplementary information** The online version contains supplementary material available at https://doi.org/10.1038/s43247-024-01256-3.

**Correspondence** and requests for materials should be addressed to Hakan Tanyas.

**Peer review information** *Communications Earth & Environment* thanks Ben Leshchinsky and the other, anonymous, reviewer(s) for their contribution to the peer review of this work. Primary Handling Editors: Joe Aslin, and Carolina Ortiz Guerrero. A peer review file is available.

**Reprints and permissions information** is available at http://www.nature.com/reprints

**Publisher's note** Springer Nature remains neutral with regard to jurisdictional claims in published maps and institutional affiliations.